Phase Evolution and Area Fractions of Coarse-Grain and Fine-Grain A15 in APC Nb_3Sn Superconductors

Fang Wan, Xingchen Xu, Xuan Peng, and Michael. D. Sumption

***Abstract*—Previous studies have shown that APC Nb_3Sn strands based on the internal oxidation of Nb-Ta-Zr or Nb-Ta-Hf alloys had higher non-Cu critical current density (J_cs) than the state-of-the-art strands at high fields (e.g., $\geq$ 12 T) while having lower non-Cu J_cs at low fields (e.g., $\leq$ 5 T), which helps to reduce the undesired persistent-current magnetization. Moreover, APC strands reacted at lower temperature tend to have flatter $J_c(B)$ curves, possibly allowing the targeting of even better J_c performance at high fields, while at the same time suppressing J_cs at low fields. However, it is required that APC strands attain large fine-grain (FG) area fractions and suppressed coarse-grain (CG) area fractions at low reaction temperature. In this work, the influence of reaction temperature on the evolution of FG and CG Nb_3Sn phases in APC Nb_3Sn strands was investigated. Our goal is to find more effective methods to increase the FG area fraction as well as the overall performance of APC strands.**

***Index Terms*—APC Nb_3Sn strands, FG/CG ratio, internal-oxidation, non-Cu J_c, reaction temperature.**

I. Introduction

Nb_3SN is a promising superconductor for the development of high-field magnets due to its high critical current density in relevant magnetic fields, relatively lower cost (compared to high-temperature superconductors), and technology maturity [1], [2], [3], [4], [5]. In the past decades, many efforts have been made to further improve the J_c performance of Nb_3Sn strands for use in the high-field magnets of circular colliders, for example the Future Circular Collider (FCC)-hh [6] which is proposed to succeed the Large Hadron Collider (LHC) [7].

It has been demonstrated that one effective method for increasing critical current density (J_c) in Nb_3Sn is the introduction of Artificial Pinning Centers (APCs) [8], [9], [10], [11], [12], [13], [14]. In 2014, Xu et al. first introduced this technique, generating a high density of APCs (ZrO_2) into their Nb_3Sn strands through the internal oxidation of Nb-Zr [13]. More recent studies have shown that APCs can also be introduced through the internal-oxidation of Nb-Ta-Hf alloy, leading to APCs based on HfO_2 nanoparticles [9], [15], [16]. In addition, the APC strands reacted at lower temperature generate flatter J_c-B curves, which has the potential to generate higher layer J_cs at a high field range ($\geq$ 12 T) while suppressing low-field layer J_cs ($\leq$ 5 T) leading to lower persistent-current magnetization [13], [14], [15], [16], [17].

The evolutions of the fine-grain (FG) and coarse-grain (CG) regions in the APC Nb_3Sn strands have not been fully studied. Only the FG layer contributes effectively to the current-carrying-capacity [18], [19], [20], [21]. Given this, the FG layer area fraction needs to be increased in order to maximize the non-Cu J_cs of Nb_3Sn strands. In this work, we describe the phase evolution sequence of APC Nb_3Sn strands during heat treatments at low temperature (650–675 °C) as well as high temperature (700–705 °C) and its influence on the A_{FG}/A_{CG} ratio and $A_{FG}/(A_{CG}+A_{Core})$ ratio. Based on these investigations, we pursued the possibility in the development of an effective method to increase both A_{FG}/A_{CG} and $A_{FG}/(A_{CG}+A_{Core})$ ratios for low reaction temperature in these APC Nb_3Sn strands.

II. Experimental

A. Samples

Two APC strands and one tube-type (TT) strand, all fabricated by Hyper Tech Research, Inc., were used for this study. The APC strands, which are denoted as "APC-Zr" and "APC-Hf", were fabricated by using ternary Nb alloys with the nominal compositions of Nb-4at.%Ta-1at.%Zr and Nb-4at%Ta-1at%Hf, respectively, and filling sufficient mixture of Sn, Cu, and SnO_2 powders into Nb filament cores, which are similar to a previous APC strand presented in [14]. Both APC strands have a 48/61 design including 48 Nb_3Sn filaments and 13 Cu rods, a Cu/non-Cu ratio of 1.15–1.25, and a diameter of 0.72 mm. The TT strand with a 54/61 design (54 Nb_3Sn filaments and 7 Cu rods) and a diameter of 0.72 mm was fabricated by using a binary Nb alloy with the nominal composition of Nb-4at%Ta and Cu-clad Sn rods filled into the cores of Nb filaments. The Cu/Sn ratio of the TT strand is similar to those of the APC strands. Transverse cross-sectional areas of the Nb_3Sn strands are shown in Fig. 1. Each strand was cut into several segments and these segments were processed with different heat-treatment conditions under vacuum. Table I illustrates sample name and heat-treatment conditions.

Received 25 September 2024; revised 28 November 2024; accepted 3 December 2024. Date of publication 9 December 2024; date of current version 24 December 2024. This work was supported by the U.S. Department of Energy through an Early Career Research Program and Hyper Tech SBIR DE-SC0017755. *(Corresponding author: Fang Wan.)*

Fang Wan and Xingchen Xu are with Fermi National Accelerator Laboratory, Batavia, IL 60510 USA (e-mail: fangwan@fnal.gov; xxu@fnal.gov).

Xuan Peng is with Hyper Tech Research, Inc., Columbus, OH 43228 USA (e-mail: xpeng@hypertechresearch.com).

Michael. D. Sumption is with the Department of Materials Science and Engineering, The Ohio State University, Columbus, OH 43210 USA (e-mail: sumption.3@osu.edu.).

Color versions of one or more figures in this article are available at https://doi.org/10.1109/TASC.2024.3513941.

Digital Object Identifier 10.1109/TASC.2024.3513941

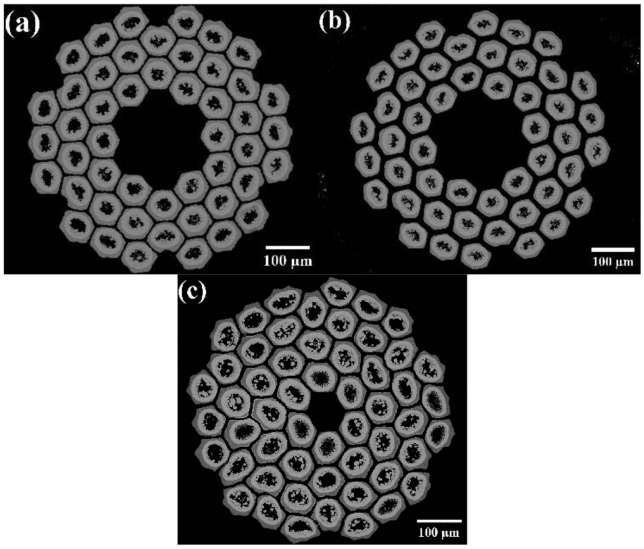

Fig. 1. BSE-SEM images of the transverse cross-sectional areas of (a) strand APC-Zr, (b) strand APC-Hf, and (c) strand TT.

TABLE I
SAMPLE NAME AND HEAT TREATMENT (H.T.) CONDITIONS

Sample	High-Temperature H.T.	Low-Temperature H.T.
APC-Zr	700°C × 1, 2, 4, 8, 16, 38 h	650°C × 6, 12, 24, 48, 96, 215 h
APC-Hf	700°C × 2.5, 3, 4, 5.5, 7 h 705°C × 85 h	650°C × 48, 72, 96, 120, 216 h 675°C × 400 h
TT	700°C × 1, 2, 4, 8, 17.5, 30.5, 38 h	650°C × 6, 12, 24, 48, 96, 215 h

B. Characterization

Transverse cross-sectional-area images of the samples were obtained using a Thermofisher Helios scanning electron microscope in the back-scattered mode (BSE-SEM) with activation energies of 20–25 kV and beam currents of 6.4–11 nA. In addition, Energy Dispersive Spectroscopy (EDS) analysis with activation energies of 20–25 kV was performed to determine the elemental compositions of the FG and CG regions of samples. The cps/eV values of main spectrum peaks for Nb, Sn, and Cu are 1000, 700, and 100–200, respectively.

C. Image Analysis

For each sample, 10 Nb_3Sn subelements in one transverse cross section were selected for image analysis and the average values and standard errors of different parameters are obtained from these subelements, an example shown in Fig. 2(a). ImageJ was used to obtain transverse areas of subelements, FG, CG, and Core region (A_{Sub}, A_{FG}, A_{CG}, and A_{Core}). These areas are shown in Fig. 2(b). In this analysis, the shapes of transverse cross-sections for subelements, (FG+CG+Core) regions, (CG+Core) regions, and Core regions were treated as circles. The subelement radius (R_{Sub}) was calculated by $\sqrt{A_{Sub}/\pi}$.

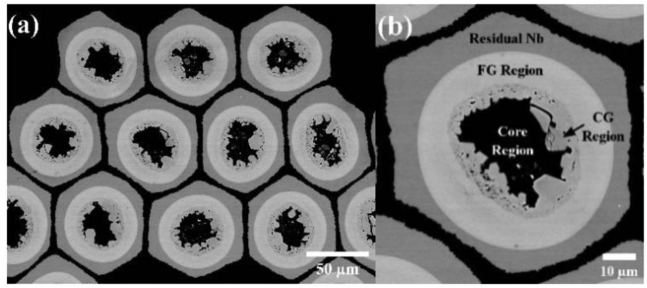

Fig. 2. BSE-SEM images of the transverse cross sections of (a) 10 Nb_3Sn subelements used for image analysis and (b) residual Nb, FG, CG, and core regions in one representative Nb_3Sn subelement.

The distances from the Nb/FG boundary, FG/CG boundary, and CG/Core boundary to subelement center ($R_{FG+CG+Core}$, $R_{CG+Core}$, R_{Core}) are equal to $\sqrt{(A_{FG}+A_{CG}+A_{Core})/\pi}$, $\sqrt{(A_{CG}+A_{Core})/\pi}$, and $\sqrt{A_{Core}/\pi}$, respectively. The normalized FG thickness (nt_{FG}) and normalized CG thickness (nt_{CG}) are calculated by $(R_{FG+CG+Core} - R_{CG+Core})/R_{Sub}$ and $(R_{CG+Core} - R_{Core})/R_{Sub}$, respectively.

III. RESULTS

A. Phase Evolutions of APC and TT Strands

It was found that the phase evolution sequence of APC strands is very similar to that of PIT and TT strands [21], [22], [23], [24], [25], [26], [27]. Fig. 3 shows the normalized layer thicknesses of all phases as a function of reaction time for (a) strand APC-Zr and (b) strand APC-Hf reacted at 700 °C and 650 °C. In Fig. 3, the y-axis shows normalized distances from the Nb/FG boundary, FG/CG boundary, CG/Core boundary to subelement center which are the distances from the Nb/FG boundary, FG/CG boundary, CG/Core boundary to the subelement center divided by subelement radius. For APCs reacted at 700 °C, we see (I) the Nb_6Sn_5 layer continued growing until the reaction time reached 2.5–4 h; simultaneously, a thin layer of FG Nb_3Sn was formed outside the Nb_6Sn_5 layer (Fig. 4(a)), (II) after that, the Nb_6Sn_5 phase decomposed into the CG Nb_3Sn phase and released free Sn atoms which diffused through the already-formed CG and FG layers into the residual Nb to form new FG layers, and the Nb_6Sn_5 phase completely decomposed into the CG Nb_3Sn when the reaction time was extended to 5.5–8 h (Fig. 4(b)), and (III) the amount of the FG layer increased to a maximum (perhaps based on the diffusion of extra Cu-Sn in the subelement core through the already-formed CG layer and FG layer into the residual Nb) (Fig. 4(c)). The phase evolution sequence at 650 °C was the same as that at 700 °C, but every stage requires a longer reaction time to complete the phase transformation. The layer thicknesses of all phases and regions as a function of reaction time for the strand TT reacted at 700 °C and 650 °C are demonstrated for comparison in Fig. 5.

As shown in Fig. 3, the normalized FG thicknesses of both APC-Zr reacted at 650 °C for 215 h and APC-Hf reacted at 700 °C for 7 h did not reach the maximum values due to not long enough reaction time. Therefore, the APC-Hf reacted at

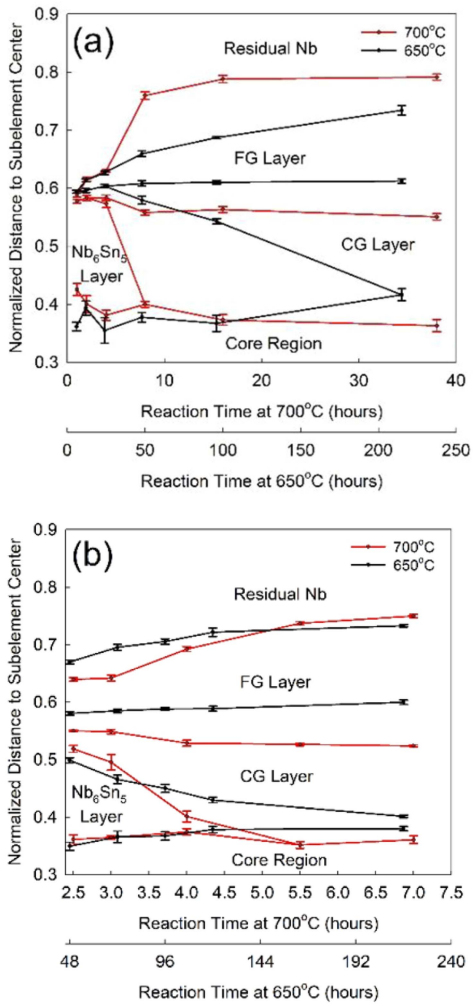

Fig. 3. Normalized distances from boundaries between different regions to subelement center as a function of reaction time for (a) the strand APC-Zr and (b) the strand APC-Hf reacted at 700 °C and 650 °C.

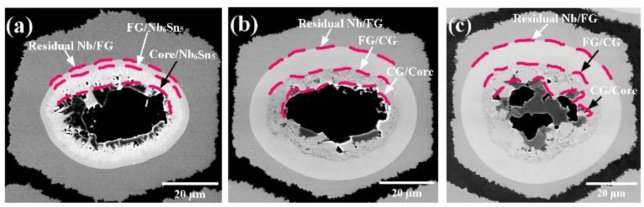

Fig. 4. BSE-SEM images of subelements for the strand APC-Zr reacted at 700 °C for (a) 4 h, (b) 8 h, and (c) 38 h.

675 °C for 400 h was selected to make a fair comparison with the APC-Hf reacted at 705 °C for 85 h. The normalized thicknesses of TT strands reacted at 700 °C for 38 h and at 650 °C for 215 h, as shown in Fig. 5, are very close to the maximum values; thus, two samples were compared with each other. The final normalized layer thicknesses of FG, CG, and Core (nt_{FG}, nt_{CG}, and nr_{Core}), and the area fraction ratios of A_{FG}/A_{CG} and $A_{FG}/(A_{CG}+A_{Core})$ were calculated for the APC-Hf strand and for the TT strand, and are summarized in Table II. For

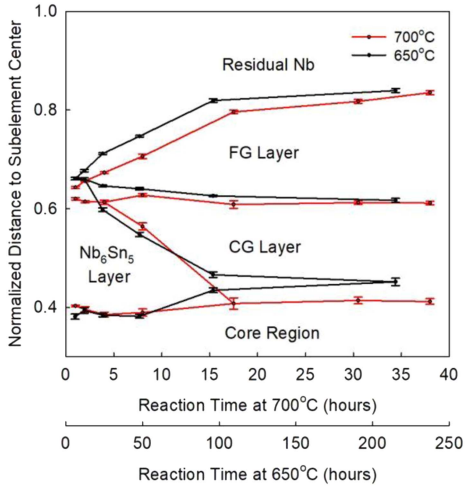

Fig. 5. Normalized distances from boundaries between different regions to subelement center as a function of reaction time for the strand TT reacted at 700 °C and 650 °C.

TABLE II
NORMALIZED THICKNESSES AND AREA FRACTION RATIOS

Para.	APC-Hf 705°C×85h	APC-Hf 675°C×400h	TT 700°C×38h	TT 650°C×215h
nt_{FG}	0.275±0.002	0.214±0.001	0.224±0.006	0.223±0.006
nt_{CG}	0.179±0.005	0.180±0.003	0.200±0.005	0.165±0.005
nr_{Core}	0.331±0.005	0.372±0.004	0.412±0.006	0.452±0.007
A_{FG}/A_{CG}	2.38±0.05	1.70±0.03	1.59±0.06	1.85±0.06
$A_{FG}/(A_{CG}+A_{Core})$	1.37±0.02	0.926±0.008	0.870±0.033	0.856±0.030

strand APC-Hf, the nt_{FG} at 705 °C is 28.5% higher than that at 675 °C, and the *ntCG* at 705 °C is close to that at 675 °C. For strand TT, the nt_{FG} at 700 °C is close to that at 650 °C. Strand APC-Hf has a larger difference in the normalized thickness of the FG layer caused by different reaction temperatures than strand TT. Consequently, compared to strand TT, the A_{FG}/A_{CG} and $A_{FG}/(A_{CG}+A_{Core})$ of the APC strand are more significantly affected by the reaction temperature, and the lower reaction temperature tends to reduce the FG relative amount and cause lower A_{FG}/A_{CG} and $A_{FG}/(A_{CG}+A_{Core})$. At the high reaction temperature ($\geq$ 700 °C), the APC strand obtains a higher FG relative amount, a smaller CG relative amount and a smaller Core relative amount than the TT strand; thus, the APC strand has larger A_{FG}/A_{CG} and $A_{FG}/(A_{CG}+A_{Core})$ than the TT strand at high reaction temperatures.

B. Connectivity of Coarse Grain Layer

Reaction temperature has an influence on CG layer thickness as well as the connectivity of the CG layer, as shown in Fig. 6. BSE-SEM images of strand APC-Zr (Fig. 6(a) and (b)) show that a high density of dark regions exists in the CG layer of samples reacted at 700 °C, while no dark regions are observed in the CG layer of samples reacted at 650 °C. These dark regions, which exist among coarse Nb_3Sn grains, define a CG layer which has become disconnected. The CG layer is well-connected in

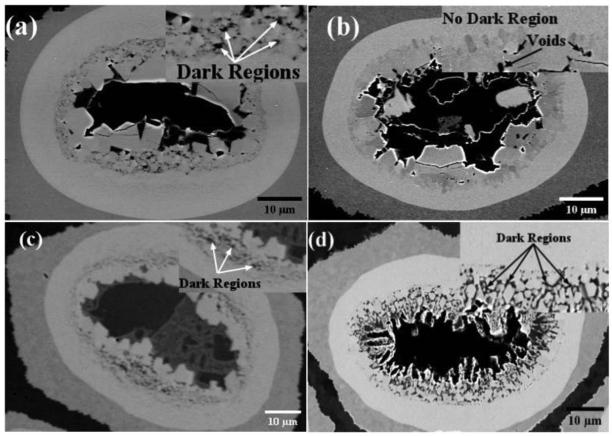

Fig. 6. BSE-SEM images of the CG layers of (a) APC-Zr reacted at 700 °C for 38 h, (b) APC-Zr reacted at 650 °C for 215 h, (c) TT reacted at 700 °C for 30.5 h, and (d) TT reacted at 650 °C for 215 h.

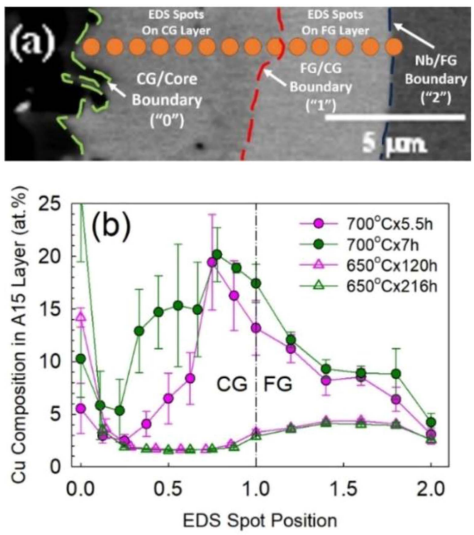

Fig. 7. (a) the diagram of EDS spots applied on the A15 phase layer. (b) Cu composition profiles of A15 layers along the radial direction of subelement for sample APC-Hf reacted at 700 °C for 5.5 h, 7 h and at 650 °C for 120 h, 216 h.

samples where the CG layer has no dark regions. The connectivity of the CG layer for APC strands is dependent on reaction temperature, with a lower reaction temperature more likely to lead to a well-connected CG layer. For strand TT, BSE-SEM images (Fig. 6(c) and (d)) show that dark regions are present in CG layers at both 650 and 700 °C. In other words, the reaction temperature has no effect on the connectivity of the CG layer for TT strands and the CG layers tend to be disconnected even at low temperature. The results of strand APC-Hf are similar to those of strand APC-Zr. EDS analysis was performed on the disconnected CG layers of APC-Hf sintered at 700 °C for 5.5 and 7 h as well as the well-connected CG layers of APC-Hf sintered at 650 °C for 120 and 216 h. As shown in Fig. 7(a), for each sample, the transverse cross sections of 3 subelements were selected and EDS spots were applied along one radial direction of each subelement. All subelements of each sample have same number of EDS spots on CG and FG layer, respectively. The Cu composition profiles of A15 layers along the radial direction of subelements are shown in Fig. 7(b). In this figure, the Cu composition on each EDS spot is the average Cu composition value with its standard error of the EDS spot with the same spot number for all of 3 subelements. On the non-linear x-axis of Fig. 7(b), the EDS spot at the boundary between the Core region and the CG layer is defined as "0", the EDS spot at the boundary between the CG layer and the FG layer is defined as "1", and the EDS spot at the boundary between the FG layer and the residual Nb region is defined as "2". It can be noticed that CG layers formed at 700 °C have much higher Cu compositions than CG layers formed at 650 °C. This result confirms that the dark regions in the disconnected CG layer are Cu-rich phases.

IV. Discussion

Above we saw that reaction temperatures $\leq$ 675 °C lead to well-connected CG layers as well as reduced FG layer thicknesses for APC Nb_3Sn strands. This result shows that the full FG layer growth of the APC strand is possibly prevented at low reaction temperature. It has been acknowledged that the Cu and Sn diffusion within the A15 is dominated by grain-boundary diffusion in Nb_3Sn conductors [20], [28], [29]. It can be speculated that a well-connected CG layer has the ability to limit Cu and Sn diffusion due to its low grain-boundary density. Consequently, the growth of the FG layer could be prevented by the well-connected CG layer. On the other hand, if the CG layer was disconnected and Cu-rich phases existed among the coarse grains, Cu and Sn diffusion would not be affected. This is because the Cu and Sn atoms can diffuse along the Cu-rich phases among Nb_3Sn coarse grains with high diffusivities. The rich-Cu phases in the CG layer might be from the decomposed Nausite [30], [31], decomposed Nb_6Sn_5, and Cu-Sn phases in subelement core region, which needs to be further explored.

V. Conclusion

This work studied the phase evolution of APC Nb_3Sn strands with a particular focus on the influence of reaction temperature on the connectivity of the CG layer, A_{FG}/A_{CG} and $A_{FG}/(A_{CG}+A_{Core})$. It was found that APC strands reacted at low temperatures have a lower FG layer area fraction (although lower reaction temperature may lead to higher layer J_c). The lower FG thickness at low reaction temperatures may be related with the formation of a well-connected CG layer at these reaction temperatures, which might impede Cu and Sn transport. In order to further enhance high-field non-Cu J_cs while retaining small low-field magnetizations, it appears to be desired to find a method to create a disconnected CG layer at low reaction temperatures.

References

[1] X. Xu, "A review and prospects for Nb_3Sn superconductor development," *Supercond. Sci. Technol.*, vol. 30, Aug. 2017, Art. no. 093001.

[2] M. B. Field, Y. Zhang, H. Miao, M. Gerace, and J. A. Parrell, "Optimizing Nb_3Sn conductors for high field applications," *IEEE Trans. Appl. Supercond.*, vol. 24, no. 3, Jun. 2014, Art. no. 6001105, doi: 10.1109/TASC.2013.2285314.

[3] F. Buta et al., "Very high upper critical fields and enhanced critical current densities in Nb_3Sn superconductors based on Nb–Ta–Zr alloys and internal oxidation," *J. Phys. Mater.*, vol. 4, Mar. 2023, Art. no. 025003.
[4] Q. Guo et al., "Study on the high temperature heat treatment process optimization of different sizes high J_c Nb_3Sn wire produced by WST," *IEEE Trans. Appl. Supercond.*, vol. 34, no. 3, May 2024, Art. no. 6001104, doi: 10.1109/TASC.2024.3363684.
[5] S. Balachandran, B. Walker, P. J. Lee, W. L. Starch, C. Tarantini, and D. C. Larbalestier, "Comparative drawability and recrystallization evaluation of Nb_4Ta and Nb_4Ta1Hf alloys, and the beneficial influence of Hf on developing finer Nb_3Sn grain size," *J. Alloys Compounds*, vol. 984, May 2024, Art. no. 173985.
[6] M. Benedikt and F. Zimmermann, "Future circular colliders," *Proc. Int. Sch. Phys.*, vol. 194, pp. 73–80, 2016.
[7] J. L Rossi and O Bruning, Eds., *High Luminosity Large Hadron Collider: The New Machine For Illuminating The Mysteries Of Universe*, vol. 24. Singapore: World Sci., 2015, doi: 10.1142/9581.
[8] T. Spina, A. Ballarino, L. Bottura, C. Scheuerlein, and R. Flukiger, "Artificial pinning in Nb_3Sn wires," *IEEE Trans. Appl. Supercond.*, vol. 27, no. 4, Jun. 2017, Art. no. 8001205, doi: 10.1109/TASC.2017.2651583.
[9] S. Balachandran et al., "Beneficial influence of Hf and Zr additions to Nb4at% Ta on the vortex pinning of Nb_3Sn with and without an O source," *Supercond. Sci. Technol.*, vol. 32, no. 4, Feb. 2019, Art. no. 044006.
[10] L. B. S. Da Silva, C. A. Rodrigues, C. Bormio-Nunes, N. F. Oliveira Jr, and D. Rodrigues, "Influence of the introduction and formation of artificial pinning centers on the transport properties of nanostructured Nb_3Sn superconducting wires," *J. Phys.: Conf. Ser.*, vol. 167, 2009, Art. no. 012012.
[11] L. R. Motowidlo, P. J. Lee, C. Tarantini, S. Balachandran, A. K. Ghosh, and D. C. Larbalestier, "An intermetallic powder-in-tube approach to increased flux-pinning in Nb_3Sn by internal oxidation of Zr," *Supercond. Sci. Technol.*, vol. 31, no. 1, Nov. 2017, Art. no. 014002.
[12] N. Paudel, C. Tarantini, S. Balachandran, W. L. Starch, P. J. Lee, and D. C. Larbalestier, "Influence of Nb alloying on Nb recrystallization and the upper critical field of Nb_3Sn," *Phys. Rev. Mater.*, vol. 8, Jul. 2024, Art. no. 084801.
[13] X. Xu, M. Sumption, X. Peng, and E. W. Collings, "Refinement of Nb_3Sn grain size by the generation of ZrO_2 precipitates in Nb_3Sn wires," *Appl. Phys. Lett.*, vol. 104, Feb. 2014, Art. no. 082602.
[14] X. Xu, X. Peng, J. Rochester, J. Lee, and M. Sumption, "High critical current density in internally-oxidized Nb_3Sn superconductors and its origin," *Scripta Materialia*, vol. 186, pp. 317–320, Jun. 2019.
[15] X. Xu et al., "The strong influence of Ti, Zr, Hf solutes and their oxidation on microstructure and performance of Nb_3Sn superconductors," *J. Alloys Compounds*, vol. 857, Mar. 2021, Art. no. 158270.
[16] X. Xu et al., "APC Nb_3Sn superconductors based on internal oxidation of Nb-Ta-Hf alloys," *Supercond. Sci. Technol.*, vol. 36, Feb. 2023, Art. no. 035012.
[17] X. Xu, M. Sumption, F. Wan, X. Peng, J. Rochester, and E. S. Choi, "Significant reduction in the low-field magnetization of Nb_3Sn superconducting strands using the internal oxidation APC approach," *Supercond. Sci. Technol.*, vol. 36, Jun. 2023, Art. no. 085008.
[18] B. Wu et al., "Effect of Nb_3Sn coarse grains on critical current densities of internal tin Nb_3Sn strand," *IEEE Trans. Appl. Supercond.*, vol. 30, no. 4, Jun. 2020, Art. no. 6000604, doi: 10.1109/TASC.2020.2970904.
[19] C. Scheuerlein et al., "Coarse Nb_3Sn grain formation and phase evolution during the reaction of a high Sn content internal tin strand," *IEEE Trans. Appl. Supcond.*, vol. 21, no. 3, pp. 2554–2558, Jun. 2011, doi: 10.1109/TASC.2010.2082476.
[20] I. Pong, L. -R. Oberli, and L. Bottura, "Cu diffusion in Nb_3Sn internal tin superconductors during heat treatment," *Supercond. Sci. Technol.*, vol. 26, no. 10, Aug. 2013, Art. no. 105002.
[21] C. Segal, C. Tarantini, P. J. Lee, and D. Larbalestier, "Improvement of small to large grain A15 ratio in Nb_3Sn PIT wires by inverted multistage heat treatments," *IOP Conf. Ser.: Mater. Sci. Eng.*, vol. 279, Jul. 2017, Art. no. 012019.
[22] C. Scheuerlein et al., "Effect of the fabrication route on the phase and volume changes during the reaction heat treatment of Nb_3Sn superconducting wires," *Supercond. Sci. Technol.*, vol. 33, no. 3, Jan. 2020, Art. no. 034004.
[23] C. Scheuerlein et al., "Phase transformations during the reaction heat treatment of Nb_3Sn superconductors," *J. Phys.: Conf. Ser.*, vol. 234, 2010, Art. no. 022032.
[24] S. Bhartiya, M. D. Sumption, X. Peng, E. Gregory, M. J. Tomsic, and E. W. Collings, "Investigation of the effects of low temperature heat treatments on the microstructure and properties of multifilamentary, tube-type Nb_3Sn strands," *IEEE Trans. Appl. Supercond.*, vol. 19, no. 3, pp. 2588–2592, Jun. 2009, doi: 10.1109/TASC.2009.2018498.
[25] X. Wu, X. Peng, M. D. Sumption, E. Gregory, M. Tomsic, and E. W. Collings, "Titanium diffusion and phase formation in tube-type rod-in-tube and internal-tin Nb_3Sn strands," *AIP Conf. Proc.*, vol. 824, pp. 504–512, Mar. 2006.
[26] X. Wu, X. Peng, M. D. Sumption, M. Tomsic, E. Gregory, and E. W. Collings, "Ti and Sn diffusion and its influence on phase formation in internal-tin Nb_3Sn superconductor strands," *IEEE Trans. Appl. Supercond.*, vol. 15, no. 2, pp. 3399–3402, Jun. 2005, doi: 10.1109/TASC.2005.848921.
[27] X. Xu, M. D. Sumption, and E. W. Collings, "A model for phase evolution and volume expansion in tube type Nb_3Sn conductors," *Supercond. Sci. Technol.*, vol. 26, Oct. 2013, Art. no. 125006.
[28] S. H. Oh, Y. J. Jeong, S. H. Na, J. Kim, A. Zargaran, and B. J. Lee, "Atomic behavior of Ti in A15 Nb_3Sn and its effects on diffusional growth of Nb_3Sn layer," *J. Alloys Compounds*, vol. 957, Sep. 2023, Art. no. 170438.
[29] X. Xu, M. D. Sumption, J. Lee, J. Rochester, and X. Peng, "Persistent compositions of non-stoichiometric compounds with low bulk diffusivity: A theory and application to Nb_3Sn superconductors," *J. Alloys Compounds*, vol. 845, Dec. 2020, Art. no. 156182.
[30] S. Martin, A. Walnsh, G. Nolze, A. Leineweber, F. Leaux, and C. Scheuerlein, "The crystal structure of $(Nb_{0.75}Cu_{0.25})Sn_2$ in the Cu-Nb-Sn system," *Intermetallics*, vol. 80, pp. 16–21, Jan. 2017.
[31] J. Lachmann, M. J. Kriegel, A. Leineweber, S. -L. Shang, and Z. -K. Liu, "Thermodynamic re-modelling of the Cu-Nb-Cu system: Integrating the nausite phase," *Calphad*, vol. 77, Jun. 2022, Art. no. 102409.